1. Grzegorz UTRATA[1], 2. Jarosław ROLEK[2]

Czestochowa University of Technology, Faculty of Electrical Engineering (1), Kielce University of Technology, Faculty of Electrical Engineering, Automatic Control and Computer Science (2)
ORCID: 1. 0000-0001-9765-8682; 2. 0000-0001-9307-5244

doi:10.15199/48.2024.07.37

The simulation studies on the induction motor sensorless field oriented control with the MRAS-based speed estimator including the rotor deep-bar effect

***Abstract**. The paper presents the selected results from the simulation studies on the induction motor (IM) speed-sensorless field oriented control. The rotor flux space vector components and rotor speed were obtained from the MRAS-based speed estimator. This estimator was formulated on the IM space vector model which enables to model the rotor impedance variability resulting from the rotor deep-bar effect by the cascade-connected two-terminal-pair networks with rotor equivalent resistances and leakage inductances.*

***Streszczenie.** W artykule zaprezentowano wybrane wyniki badań symulacyjnych bezczujnikowego polowo-zorientowanego układu regulacji prędkości kątowej silnika indukcyjnego (SI). Składowe wektora przestrzennego strumienia wirnika oraz prędkość kątowa odtwarzane były w tym układzie za pomocą estymatora typu MRAS. Estymator ten został sformułowany na podstawie modelu matematycznego SI z wieloobwodowym odwzorowaniem zmienności impedancji wirnika wynikającej ze zjawiska wypierania prądu **(Badania symulacyjne bezczujnikowego układu napędowego z estymatorem typu MRAS uwzględniającym zmienność impedancji wirnika silnika indukcyjnego wynikającą ze zjawiska wypierania prądu)**.*

Keywords: induction motors, variable speed drives, state estimation, deep-bar effect.
Słowa kluczowe: silniki indukcyjne, układy napędowe, estymacja, wypieranie prądu.

Introduction

The field oriented control of induction motors (IMs) assure the wide-range speed control with maintaining the motor slip frequency over the assumed operating point. The exception to that are short transients occurring over rapid load torque disturbances or speed commands [1]. As the slip frequency changes, the rotor impedance varies due to the rotor deep-bar effect.

Various estimation methods for the rotor flux space vector and rotor speed have been proposed in the literature [2-5]. A good part of these works were devoted to methods developed on IM space vector models where the rotor impedance was represented by a series rotor equivalent resistance and leakage inductance (the commonly use T-type equivalent circuit). The equivalent circuit parameters of these models are generally determined in the assumed operating point. Therefore such a model could not be suitable for proper modelling of the rotor impedance variability when the slip frequency deviates from its rated value in such a way that the wider range of slip frequency changes the greater inaccuracy of the rotor impedance variability representation is possible. This, in turn, affects the precision of rotor flux and speed estimation. In order to provide the desirable dynamics of the IM speed-sensorless rotor flux oriented control during transients, it could be justified to employ it with the rotor flux and speed estimation systems which would also take into account the rotor impedance variability resulting from the rotor deep-bar effect [6].

Numerous studies on designing of the IM space vector models and on identifying their equivalent circuit parameters to represent the rotor impedance variability occurred with slip frequency changes have been published up to now, i.a. [7-10]. However, only a few works dealt with the use of such a model for the field oriented controlled IM drives [1, 6, 11-14]. The literature lacks in studies on the IM speed-sensorless rotor flux oriented control where the rotor flux space vector components and rotor speed are obtained by an estimation system which would be developed on the IM space vector model including the rotor deep-bar effect. This paper is a step towards filling in this gap.

IM space vector models including rotor deep-bar effect

The literature presents the IM space vector models with different types of two-terminal-pair networks connected in cascade for modelling the rotor impedance variability resulted from the rotor deep-bar effect [7-10]. The choice of the two terminal-pair network type and the number N of this networks connected in cascade within the rotor equivalent circuit is related to accuracy of the rotor impedance variability modelling in the considered range of slip frequency and the complexity of the IM space vector model [8].

The range of slip frequency changes occurred under typical operation conditions of the field oriented controlled IMs is concentrated around the assumed operating point. The desired approximation accuracy of the rotor impedance variability in such a slip frequency range can be assuredly achieved by the two ($N = 2$) cascade-connected two terminal-pair networks composed of rotor equivalent resistance and leakage inductance, e.g. the admittance type (I-type) networks or the mirror Γ-type networks.

The IM space vector model where the rotor impedance variability is modelled by two cascade-connected I-type networks is described by (1)-(4). The model with rotor represented by two cascade-connected mirror Γ-type networks is delineated by (1)-(2) and (5)-(6). The stator voltage (1) and flux (2) equations and also the electromagnetic torque (7) and speed (8) equations are the same for the both considered IM space vector models. These models can equally model the IM dynamic despite the different rotor voltage and flux equations and rotor equivalent circuit parameters. Figure 1 presents the IM equivalent circuits corresponding to these IM space vector models.

(1) $$\underline{U}_{1\mathrm{k}} = R_1 \underline{I}_{1\mathrm{k}} + \frac{\mathrm{d}}{\mathrm{d}t}\underline{\Psi}_{1\mathrm{k}} + \mathrm{j}\omega_{\mathrm{k}}\underline{\Psi}_{1\mathrm{k}}$$

(2) $$\underline{\Psi}_{1\mathrm{k}} = L_1 \underline{I}_{1\mathrm{k}} + L_{\mathrm{m}} \underline{I}_{2\mathrm{k}}$$

(3) $$\begin{cases} 0 = R^{\mathrm{I}}_{2(1)} \underline{I}^{\mathrm{I}}_{2(1)\mathrm{k}} + \dfrac{\mathrm{d}}{\mathrm{d}t}\underline{\Psi}^{\mathrm{I}}_{2(1)\mathrm{k}} + \mathrm{j}\omega_{\mathrm{x}}\,\underline{\Psi}^{\mathrm{I}}_{2(1)\mathrm{k}} \\ 0 = R^{\mathrm{I}}_{2(2)} \underline{I}^{\mathrm{I}}_{2(2)\mathrm{k}} + \dfrac{\mathrm{d}}{\mathrm{d}t}\underline{\Psi}^{\mathrm{I}}_{2(2)\mathrm{k}} + \mathrm{j}\omega_{\mathrm{x}}\,\underline{\Psi}^{\mathrm{I}}_{2(2)\mathrm{k}} \end{cases}$$

(4) $$\begin{cases} \underline{\Psi}^{\mathrm{I}}_{2(1)\mathrm{k}} = L_{\mathrm{m}}\left(\underline{I}_{1\mathrm{k}} + \underline{I}_{2\mathrm{k}}\right) + L^{\mathrm{I}}_{\sigma 2(1)}\underline{I}^{\mathrm{I}}_{2(1)\mathrm{k}} \\ \underline{\Psi}^{\mathrm{I}}_{2(2)\mathrm{k}} = L_{\mathrm{m}}\left(\underline{I}_{1\mathrm{k}} + \underline{I}_{2\mathrm{k}}\right) + L^{\mathrm{I}}_{\sigma 2(2)}\underline{I}^{\mathrm{I}}_{2(2)\mathrm{k}} \end{cases}$$

(5) $$\begin{cases} 0 = R^{\Gamma}_{2(1)}\underline{I}^{\Gamma}_{2(1)\mathrm{k}} + \dfrac{\mathrm{d}}{\mathrm{d}t}\underline{\Psi}^{\Gamma}_{2(1)\mathrm{k}} + \mathrm{j}\omega_{\mathrm{x}}\,\underline{\Psi}^{\Gamma}_{2(1)\mathrm{k}} \\ 0 = R^{\Gamma}_{2(2)}\underline{I}^{\Gamma}_{2(2)\mathrm{k}} + \dfrac{\mathrm{d}}{\mathrm{d}t}\underline{\Psi}^{\Gamma}_{2(2)\mathrm{k}} + \\ \quad + \mathrm{j}\omega_{\mathrm{x}}\left(\underline{\Psi}^{\Gamma}_{2(1)\mathrm{k}} + L^{\Gamma}_{2(2)\mathrm{k}}\underline{I}^{\Gamma}_{2(2)\mathrm{k}}\right) \end{cases}$$

(6) $$\begin{cases} \underline{\Psi}^{\Gamma}_{2(1)\mathrm{k}} = L_{\mathrm{m}}\underline{I}_{1\mathrm{k}} + \left(L_{\mathrm{m}} + L^{\Gamma}_{\sigma 2(1)}\right)\underline{I}_{2\mathrm{k}} \\ \underline{\Psi}^{\Gamma}_{2(2)\mathrm{k}} = \underline{\Psi}^{\Gamma}_{2(1)\mathrm{k}} + L^{\Gamma}_{\sigma 2(2)}\underline{I}^{\Gamma}_{2(2)} \end{cases}$$

(7) $$T_{\mathrm{em}} = \mathrm{Im}\left(\underline{\Psi}^{*}_{1\mathrm{k}}\underline{I}_{1\mathrm{k}}\right)$$

(8) $$\frac{\mathrm{d}\omega_{\mathrm{m}}}{\mathrm{d}t} = \frac{p}{J}\left(T_{\mathrm{em}} - T_{\mathrm{L}}\right)$$

where: $\underline{U}_{1\mathrm{k}}$, $\underline{I}_{1\mathrm{k}}$, $\underline{\Psi}_{1\mathrm{k}}$ – stator voltage, current, and flux space vectors, respectively; R_1, L_1 – stator resistance and inductance, respectively; $L_1 = L_{\sigma 1} + L_{\mathrm{m}}$; $L_{\sigma 1}$ – stator leakage inductance; L_{m} – magnetizing inductance; $\underline{I}_{2(n)\mathrm{k}}$, $\underline{\Psi}_{2(n)\mathrm{k}}$ – rotor current and flux space vectors, respectively, related to the n-th cascade-connected two terminal-pair networks, $n = 1, 2$; $R_{2(n)}$, $L_{\sigma 2(n)}$ – rotor equivalent resistance and leakage inductance, respectively; T_{em}, T_{L} – electromagnetic and load torque, respectively; p – pole pairs; J – mass moment of inertia; $\omega_{\mathrm{x}} = \omega_{\mathrm{k}} - \omega_{\mathrm{m}}$; ω_{m} – electrical angular speed; subscript "k" denotes space vectors expressed in an orthogonal coordinate system rotating at an arbitrary angular speed ω_{k}; superscripts "I" and "Γ" indicate rotor space vectors and equivalent circuit parameters related to the I-type and mirror Γ-type networks, respectively; * denotes the complex conjugate; $\mathrm{j}^2 = -1$.

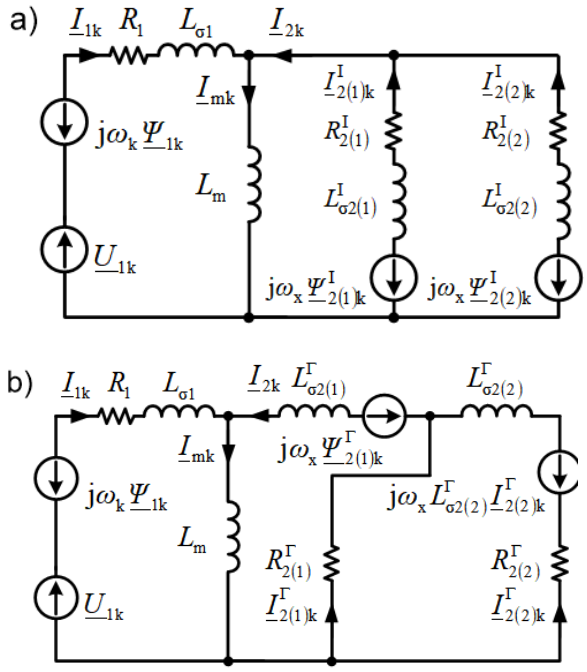

Fig. 1. The IM equivalent circuits where the rotor impedance variability is modelled by the two cascade-connected two-terminal-pair networks: a) the I-type networks; b) the mirror Γ-type networks.

Rotor flux space vector models

The space vector model with the rotor representation by the cascade-connected I-type networks provides the rotor flux space vector which can be applicable for the IM field oriented control [14]:

(9) $$\underline{\Psi}^{\mathrm{Ie}}_{2\mathrm{s}} = L^{\mathrm{I}}_{\sigma 2\mathrm{T}}\sum_{n=1}^{N}\frac{\underline{\Psi}^{\mathrm{Ie}}_{2(n)\mathrm{s}}}{L^{\mathrm{I}}_{\sigma 2(n)}}$$

(10) $$\frac{1}{L^{\mathrm{I}}_{\sigma 2\mathrm{T}}} = \sum_{n=1}^{N}\frac{1}{L^{\mathrm{I}}_{\sigma 2(n)}}$$

The subscript "s" denotes space vectors expressed in the stator coordinate system.

In that case, the rotor flux current model can be defined with substituting the following expressions for the rotor currents related to the individual cascade-connected I-type networks into the system of equations (3) expressed in the stator coordinate system:

(11) $$\underline{I}^{\mathrm{I}}_{2(1)\mathrm{s}} = \frac{1}{L^{\mathrm{I}}_{2(1)}L^{\mathrm{I}}_{2(2)} - L^{2}_{\mathrm{m}}}\begin{pmatrix} L^{\mathrm{I}}_{2(2)}\underline{\Psi}^{\mathrm{I}}_{2(1)\mathrm{s}} - L_{\mathrm{m}}\underline{\Psi}^{\mathrm{I}}_{2(2)\mathrm{s}} + \\ - L_{\mathrm{m}}\left(L^{\mathrm{I}}_{2(2)} - L_{\mathrm{m}}\right)\underline{I}_{1\mathrm{s}} \end{pmatrix}$$

(12) $$\underline{I}^{\mathrm{I}}_{2(2)\mathrm{s}} = \frac{1}{L^{\mathrm{I}}_{2(1)}L^{\mathrm{I}}_{2(2)} - L^{2}_{\mathrm{m}}}\begin{pmatrix} L^{\mathrm{I}}_{2(1)}\underline{\Psi}^{\mathrm{I}}_{2(2)\mathrm{s}} - L_{\mathrm{m}}\underline{\Psi}^{\mathrm{I}}_{2(1)\mathrm{s}} + \\ - L_{\mathrm{m}}\left(L^{\mathrm{I}}_{2(1)} - L_{\mathrm{m}}\right)\underline{I}_{1\mathrm{s}} \end{pmatrix}$$

(13) $$L^{\mathrm{I}}_{2(n)} = L_{\mathrm{m}} + L^{\mathrm{I}}_{\sigma 2(n)}\Big|_{n=1,2}$$

In another approach, when the rotor equivalent circuit currents are substituted in (3) by the following equation:

(14) $$\underline{I}^{\mathrm{I}}_{2(n)\mathrm{s}} = \frac{1}{L^{\mathrm{I}}_{\sigma 2(n)}}\left(\underline{\Psi}^{\mathrm{I}}_{2(n)\mathrm{s}} - L_{\mathrm{m}}\underline{I}_{\mathrm{ms}}\right)\Big|_{n=1,2}$$

the rotor flux voltage-current model is defined where the rotor flux space vectors related to the individual cascade-connected I-type networks become:

(15) $$\frac{\mathrm{d}}{\mathrm{d}t}\underline{\Psi}^{\mathrm{Ie}}_{2(n)\mathrm{s}} = \frac{R^{\mathrm{I}}_{2(n)}}{L^{\mathrm{I}}_{\sigma 2(n)}}\left(L_{\mathrm{m}}\underline{I}^{\mathrm{e}}_{\mathrm{ms}} - \underline{\Psi}^{\mathrm{Ie}}_{2(n)\mathrm{s}}\right) + \mathrm{j}\omega_{\mathrm{m}}\underline{\Psi}^{\mathrm{Ie}}_{2(n)\mathrm{s}}\Big|_{n=1,2}$$

and the magnetizing current I_{ms} is determined from the stator voltage (1) and flux (2) equations:

(16) $$\underline{I}^{\mathrm{e}}_{\mathrm{ms}} = \frac{1}{L_{\mathrm{m}}}\left(\int_0^t\left(\underline{U}_{1\mathrm{s}} - R_1\underline{I}_{1\mathrm{s}}\right)\mathrm{d}t - L_{\sigma 1}\underline{I}_{1\mathrm{s}}\right)$$

Based on the stator voltage (1) and flux (2) equations the rotor flux voltage model can be defined:

(17) $$\underline{\Psi}^{\mathrm{Ie}}_{2\mathrm{s}} = \frac{L^{\mathrm{I}}_{2}}{L_{\mathrm{m}}}\left(\int_0^t\left(\underline{U}_{1\mathrm{s}} - R_1\underline{I}_{1\mathrm{s}}\right)\mathrm{d}t - \sigma^{\mathrm{I}}L_1\underline{I}_{1\mathrm{s}}\right)$$

(18) $$\sigma^{\mathrm{I}} = 1 - \frac{L^{2}_{\mathrm{m}}}{L_1 L^{\mathrm{I}}_{2}}$$

(19) $$L^{\mathrm{I}}_{2} = L_{\mathrm{m}} + L^{\mathrm{I}}_{\sigma 2\mathrm{T}}$$

MRAS-based speed estimator

The model reference adaptive system (MRAS) was effectively adopted for the IM speed estimator in [15]. This estimator was formulated on the IM space vector model

with the rotor equivalent circuit in the form of the series connection of the rotor equivalent resistance and leakage inductance (the commonly used IM T-type equivalent circuit).

The MRAS concept was also employed in developing the speed estimator based on the IM space vector model with the rotor impedance variability modelled by the cascade-connected I-type networks [14]. Under this approach, analogously as in [15], the rotor flux voltage model (17) can play the role of the reference model because it is not speed dependent. On the other hand, the rotor flux current model (eqs. (3), (9), (11), (12)) or voltage-current model (eqs. (3), (9), (15), (16)) include the rotor speed and so they can be applied as the adjustable model. The synthesis technique for the MRAS-based speed estimator capable to model the rotor impedance variability was carried out by adopting the technique described in [15]. Therefore, the IM speed estimate can be tuned like in [15] through the proportional plus integral (PI) controller driven by the error signal proportional to the angular displacement between the rotor flux estimates which are determined by the reference and adjustable models. The general schematic diagram of the MRAS-based speed estimator is presented in Figure 2. In this figure, the character "^" is used to distinguish the rotor flux space vector components generated through the adjustable model form those determined by the reference one and the dashed line concerns the case when the rotor flux voltage-current model is employed as the adjustable model.

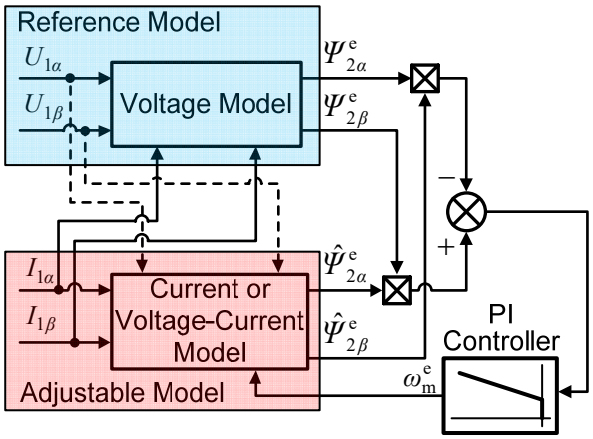

Fig. 2. The general schematic diagram of the MRAS-based speed estimator

Identification of IM equivalent circuit parameters

The equivalent circuit parameters of the IM space vector models with the rotor impedance variability represented by the cascade-connected I-type and mirror Γ-type networks were identified according to the procedure described in [10]. This procedure is carried on with using the search-based optimisation techniques where the equivalent circuit parameters are determined through matching the IM reference inductance frequency characteristic by the one resulted from the space vector model.

In the presented studies, the reference inductance frequency characteristic of the tested IM of type Sg 132S-4 were calculated based on the measurement data derived under the load curve test which was conducted according to the standard [16].

The adopted criterion for the equivalent circuit parameters' identification assumed the approximation of the reference characteristic modulus with an error not exceeding 1% in the considered slip frequency range. This range is defined under the load curve test [16] and corresponds to the load current adjustment range from the no-load current to around 1.25 of the IM rated current. The criterion also imposed a possible minimum approximation error of the reference characteristic argument with the assumed two cascade-connected two-terminal-pair networks in the rotor equivalent circuit. The reference characteristic is presented in Figure 3 together with the ones resulted from the space vector models with the rotor impedance variability modelled by the two cascade-connected I-type and the mirror Γ-type networks. For comparison, Figure 3 also includes the inductance frequency characteristic calculated from the space vector model with the rotor equivalent circuit in the form of the series connection of the rotor equivalent resistance and leakage inductance.

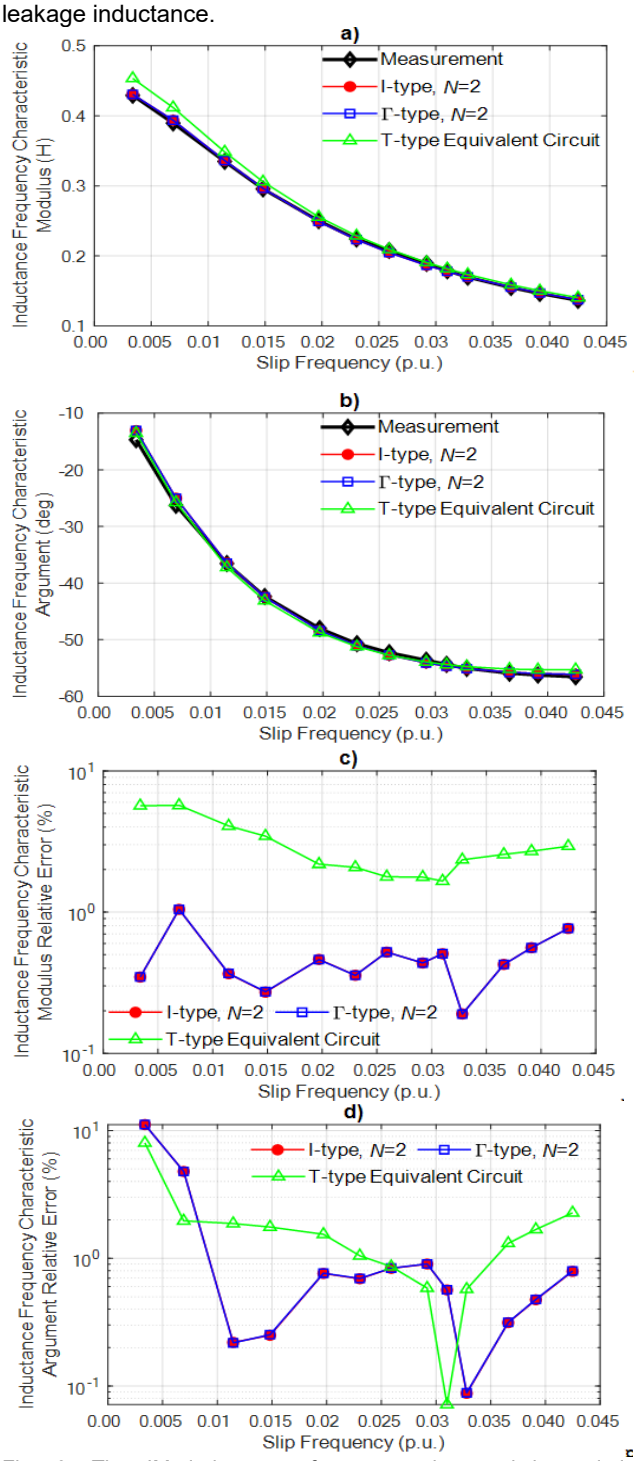

Fig. 3. The IM inductance frequency characteristic and its approximation by the space vector models: a) modulus; b) argument; c) modulus relative errors; d) argument relative errors

The T-type equivalent circuit parameters were determine on the measurement data obtained under the no-load and the load curve tests performed in line with the procedure reported in [16]. The equivalent circuit parameters of the considered space vector models are listed in Table1.

The use of the space vector model with the rotor equivalent circuit in the form of the two cascade-connected I-type or the mirror Γ-type networks allows for approximation of the reference inductance frequency characteristic modulus with the desirable accuracy in the slip frequency range which occurs under typical IM operation conditions. The accurate approximation of the reference characteristic argument is also obtained. The relative error does not exceed 1% except for the two measurement points for the tested IM operated under no-lad and light-load conditions.

Table 1. Equivalent circuit parameters at the temperature of about 50ºC

Equivalent circuit with I-type network rotor representation						
R_1 (Ω)	$L_{\sigma 1}$ (H)	L_{m} (H)	$R^{\mathrm{I}}_{2(1)}$ (Ω)	$L^{\mathrm{I}}_{\sigma 2(1)}$ (H)	$R^{\mathrm{I}}_{2(2)}$ (Ω)	$L^{\mathrm{I}}_{\sigma 2(2)}$ (H)
3.1815	0.0217	0.4228	6.0177	0.1081	2.6262	0.0219
Equivalent circuit with mirror Γ-type network rotor representation						
R_1 (Ω)	$L_{\sigma 1}$ (H)	L_{m} (H)	$R^{\Gamma}_{2(1)}$ (Ω)	$L^{\Gamma}_{\sigma 2(1)}$ (H)	$R^{\Gamma}_{2(2)}$ (Ω)	$L^{\Gamma}_{\sigma 2(2)}$ (H)
3.1815	0.0217	0.4228	2.1603	0.0171	11.8966	0.1445
T-type equivalent circuit						
R_1 (Ω)	$L_{\sigma 1}$ (H)	L_{m} (H)	R_2 (Ω)	$L_{\sigma 2}$ (H)	–	–
3.1815	0.0190	0.4503	1.8928	0.0284	–	–

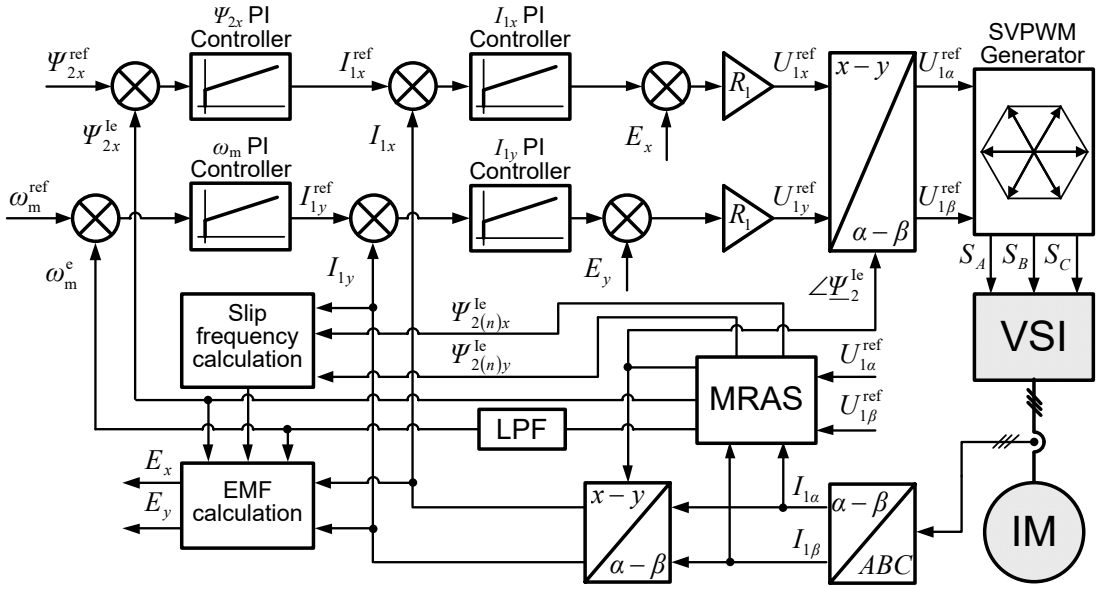

Fig. 4. The schematic diagram of the IM speed-sensorless rotor flux oriented control

Simulation of the IM sensorless rotor flux oriented control

The simulation studies were conducted with the use of the Matlab/Simulink environment. The schematic diagram of the investigated IM speed-sensorless rotor flux oriented control is presented in Figure 4. The IM space vector models with the rotor equivalent circuit in the form of the two cascade-connected I-type and the mirror Γ-type networks were employed in these studies. The first of them was used to formulate the MRAS-based speed estimator according to [14]. The latter was operated as the IM in the drive simulation model. As a result, the estimator and the IM were realised in the simulation studies by the two different space vector models of the tested IM.

The IM drive simulation model was composed from two subsystems. The first subsystem, including the IM and voltage source inverter (VSI) models, operated at the sampling period of 2 μs (the grey blocks in Figure 4). The second one, executing the speed-sensorless rotor flux oriented control, operated at the sampling period of 100 μs. This was done to make the simulation model reflected the real IM drive more closely since the digital signal processors operate with the limited sampling frequency. The switching frequency of the VSI controlled by the space vector pulse width modulation (SVPWM) was equal to 10 kHz.

The slip frequency which is required for the electromotive force (EMF) calculation was determined by (20) with the rotor flux space vector and the rotor equivalent circuit parameters related to one of the two cascade-connected I-type networks, i.e. for $n = 1$ or $n = 2$.

$$\omega_{\mathrm{slip}} = \frac{I_{1y}}{\Psi^{\mathrm{Ie}}_{2(n)x}} \frac{R^{\mathrm{I}}_{2(n)}}{L^{\mathrm{I}}_{\sigma 2(n)}} L_{\mathrm{m}} \left(1 - \frac{L_{\mathrm{m}}}{L^{\mathrm{I}}_{2}}\right) + \\ - \frac{\Psi^{\mathrm{Ie}}_{2(n)y}}{\Psi^{\mathrm{Ie}}_{2(n)x}} \frac{R^{\mathrm{I}}_{2(n)}}{L^{\mathrm{I}}_{\sigma 2(n)}} - \frac{1}{\Psi^{\mathrm{Ie}}_{2(n)x}} \frac{\mathrm{d}}{\mathrm{d}t} \Psi^{\mathrm{Ie}}_{2(n)y} \tag{20}$$

The subscripts "x" and "y" indicate the space vector components in the rotor flux oriented coordinate system.

The rotor flux voltage-current model was employed as the adjustable model of the MRAS-based speed estimator. This rotor flux model proved the better performance when

compared to the current model. The rotor flux estimated by the voltage model of the MRAS-based speed estimator was used for field orientation. It is reasoned since the presented studies did not consider the IM low speed operation where the rotor flux voltage model exhibits some drawbacks related to open loop integration [2]. The main attention of these studies was focused over the IM drive performance under slip frequency variations. For this reason, the simulation studies of the IM drive operation under the rapid load torque and reference speed changes were conducted.

Figure 5 presents the results from the simulation studies on the investigated IM drive operated under the rapid load torque disturbances. Figure 5 a) presents the reference speed, the speed obtained from the space vector model with the rotor equivalent circuit in the form of the two cascade-connected mirror Γ-type networks and the estimated speed. The time plots of the stator current space vector components in the rotor flux oriented coordinate system are presented in Figure 5 b) together with the commanded load torque. Figures 5 c) and 5 d) include the speed estimation and speed regulation relative errors calculated according to the formulas (21) and (22), respectively. Figure 6 presents the analogous time plots but for the case of the investigated IM drive operated under the rapid reference speed changes. Figure 7 includes the time plots of the slip frequency determined in line with (20) to indicate the range of its variations during the considered IM operation conditions.

(21) $$\Delta\omega_{\mathrm{m}} = \frac{\omega_{\mathrm{m}}^{\mathrm{ref}} - \omega_{\mathrm{m}}}{\omega_{\mathrm{m}}^{\mathrm{ref}}} 100\%$$

(22) $$\Delta\omega_{\mathrm{m}}^{\mathrm{e}} = \frac{\omega_{\mathrm{m}} - \omega_{\mathrm{m}}^{\mathrm{e}}}{\omega_{\mathrm{m}}} 100\%$$

where: $\omega_{\mathrm{m}}^{\mathrm{ref}}$ – reference speed, ω_{m} – IM model speed, $\omega_{\mathrm{m}}^{\mathrm{e}}$ – estimated speed.

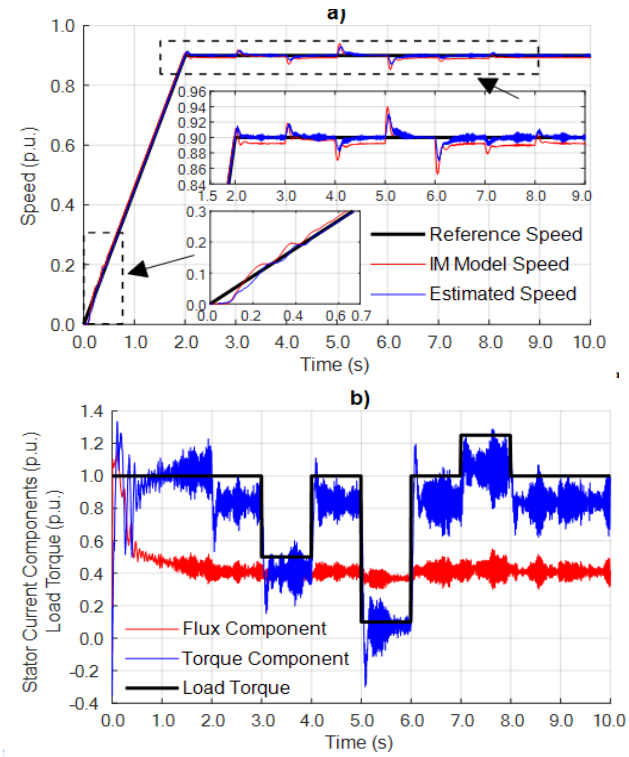

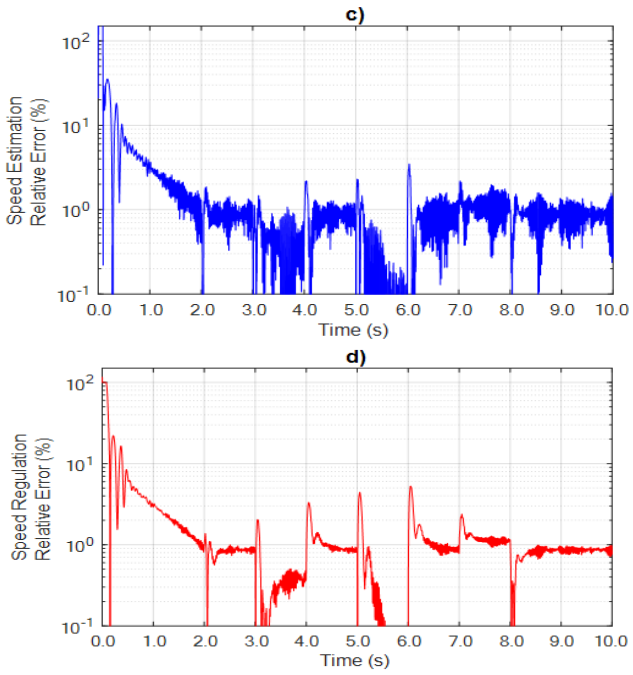

Fig. 5. The results from the simulations studies – rapid load torque changes. The time plots: a) reference, IM model and estimated speed; b) stator current space vector components and load torque; c) speed estimation relative error; d) speed regulation relative error

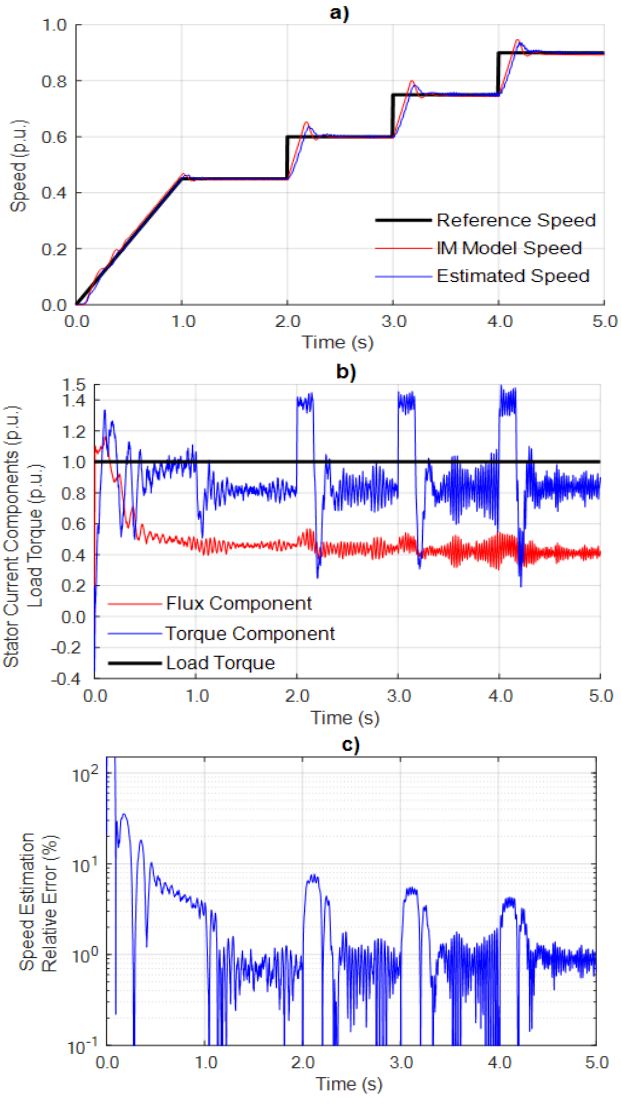

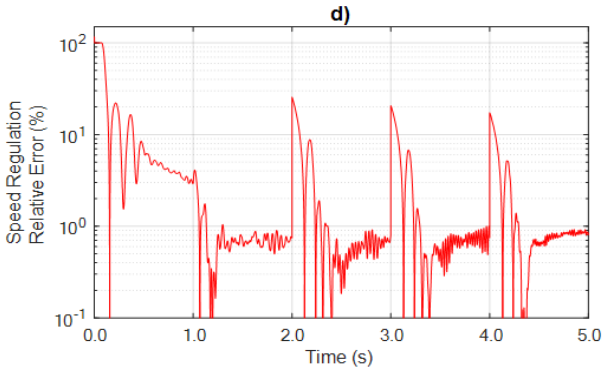

Fig. 6. The results from the simulations studies – rapid reference speed changes. The time plots: a) reference, IM model and estimated

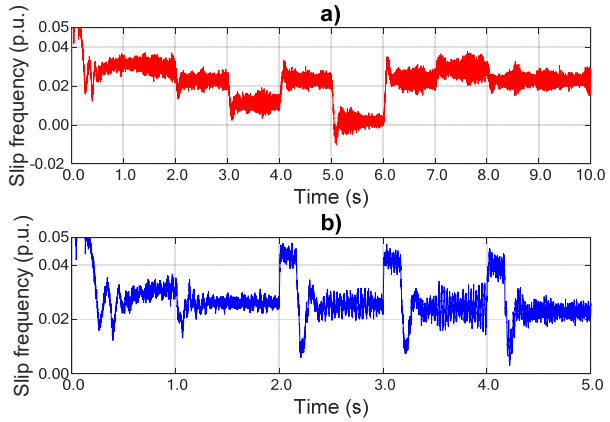

Fig. 7. The time plots of the slip frequency: a) under load torque disturbances; b) under reference speed changes

The proper operation of the MRAS-based speed estimator, which was developed on the IM space vector model including the deep-bar effect, is observed (Fig. 5 a) and 6 a)) despite of the slip frequency variations in the fairly wide range of about (0 - 0.045) (p.u.) from its rated value of about 0.022 (p.u.) (Fig. 7). The speed estimation relative errors are less than 8% during load torque and speed transients after IM start-up is finished (Fig. 5 c) and 6 c)). It should be noted that these errors are also affected by the delay introduced by the estimated speed low-pass filter (LPF) which is indispensable for the correct operation of the speed-sensorless IM drive. The speed estimation relative errors are about 1% during IM steady state operation.

The accurate rotor flux and speed estimation results in the correct operation of the investigated IM speed-sensorless rotor flux oriented control. The proper decoupling of the rotor flux and electromagnetic torque control paths is observed in Figures 5 b) and 6 b). The torque component of the stator current space vector follows closely the load torque changes in Figure 5 b) and the speed error in Figure 6 b). At the same time, the flux component is maintained constant after IM start-up is finished. As the final result, the accurate speed regulation is achieved. Its relative errors are not exceeding 5% under load torque disturbances and they are about 1% during IM steady state operation after start-up is finished (Fig. 5 d). The speed relative errors during reference speed changes are obviously greater since they are related to the reference speed step change of 0.15 (p.u.) adopted in the simulation studies (Fig. 6 d).

Conclusions

The paper presents the results of the simulation studies on the IM speed-sensorless rotor flux oriented control with the MRAS-based speed estimator including the rotor deep-bar effect. Such an estimator provided the accurate rotor flux and speed estimation under the slip frequency variations confirming its usefulness and capability to properly model the rotor impedance variability resulted from the rotor deep-bar effect. However, the experimental studies are essential to validate the usefulness of the investigated MRAS-based speed estimator for the IM speed-sensorless rotor flux oriented control. Moreover, further research is needed in order to develop the more sophisticated estimation systems including the rotor deep-bar effect which would provide the IM wide-range speed operation.

***Authors**: Grzegorz Utrata, Czestochowa University of Technology, Faculty of Electrical Engineering, 17 Armii Krajowej Ave., 42-200 Czestochowa, Poland, E-mail: grzegorz.utrata@pcz.pl; Jarosław Rolek, Kielce University of Technology, Faculty of Electrical Engineering, Automatic Control and Computer Science, 7 Tysiaclecia Panstwa Polskiego Ave., 25-314 Kielce, Poland, E-mail: jrolek@tu.kielce.pl.*

REFERENCES

[1] Seok J.-K., Sul, S.-K., Pseudorotor-flux-oriented control of an induction machine for deep-bar-effect compensation, *IEEE Trans. Ind. Appl.*, 34 (1998), 429–434
[2] Holtz J., Sensorless control of induction machines—With or without signal injection? *IEEE Trans. Ind. Electron.*, 53 (2008), 7–30.
[3] H. K. Khalil, E. G. Strangas, S. Jurkovic, Speed Observer and Reduced Nonlinear Model for Sensorless Control of Induction Motors, IEEE Trans. on Control Systems Technology, Vol. 17 (2009), Iss. 2, 327 - 339.
[4] T. Białoń, A. Lewicki, R. Niestrój, M. Pasko, Stability of a proportional observer with additional integrators on the example of the flux observer of induction motor, Przegląd Elektrotechniczny, R. 87 (2011), nr 4, 142-145.
[5] G.-J. Jo; J.-W. Choi, Gopinath Model-Based Voltage Model Flux Observer Design for Field-Oriented Control of Induction Motor, IEEE Trans. on Power Electronics, Vol. 45 (2019), Iss. 5, 4581-4592.
[6] M. J. Durán, J. L. Durán, F. Pérez, J. Fernández, Induction-Motor Sensorless Vector Control With Online Parameter Estimation and Overcurrent Protection, IEEE Trans. on Ind. Electron., vol. 53 (2006), no. 1, 154-161.
[7] D.S. Babb, J.E. Williams, Network analysis of A-C machine conductors, Trans. of the American Institute of Electrical Engineers, vol. 70 (1951), no. 2, 2001–2005.
[8] Levy W., Landy C.H., McCulloch M.D., Improved models for the simulation of deep bar induction motors, *IEEE Trans. Energy Convers.*, 2 (1990), 393–400.
[9] H.V. Khang, A. Arkkio, Parameter estimation for a deep-bar induction motor, IET Electric Power Applications, Vol. 6 (2012), Iss. 2, 133–142.
[10] J. Rolek, G. Utrata, An identification procedure of electromagnetic parameters for an induction moto equivalent circuit including rotor deep bar effect. *Arch. Electr. Eng.*, 2 (2018), 279–291.
[11] R.W. De Doncker, Field-oriented controllers with rotor deep bar compensation circuits, *IEEE Trans. Ind. Appl.*, 5 (1992), 1062–1071.
[12] R.C. Healey, S. Williamson, A.C. Smith, Improved cage rotor models for vector controlled induction motors. *IEEE Trans. Ind. Appl.*, 4 (1995), 812–822.
[13] E. Mölsä, S.E. Saarakkala, M. Hinkkanen, A. Arkkio, M. Routimo, A Dynamic Model for Saturated Induction Machines with Closed Rotor Slots and Deep Bars. *IEEE Trans. Energy Convers.*, 35 (2020), 157–165.
[14] G. Utrata, J. Rolek, The Induction Motor MRAS-Based Speed Estimator Capable of Modelling the Slip Frequency Dependent Variability of the Rotor Impedance, *Energies*, 16(6) (2023).
[15] C. Schauder, Adaptive speed identification for vector control of induction motors without rotational transducers, IEEE Trans. Ind. Appl., 28 (1992), 1054–1061.
[16] PN-EN 60034-28: 2013 Rotating Electrical Machines – Part 28: Test Methods for Determining Quantities of Equivalent Circuit Diagrams for Three-Phase Low Voltage Cage Induction Motors. Polski Komitet Normalizacyjny: Warszawa, Poland, 2013.